Method to image high-order harmonic generation and quantum trajectories in the real-time–frequency domain

Pengfei Lan and Peixiang Lu*
[1]*Wuhan National Laboratory for Optoelectronics, Huazhong University of Science and Technology, Wuhan 430074, People's Republic of China*
(Received 27 September 2007; published 11 January 2008)

High-order harmonic generation (HHG) in a near infrared driving laser pulse by mixing a weak ultraviolet pulse is investigated and a different concept of attosecond temporal filter is proposed. We show that this temporal filter can be used to (i) select the specific high-order harmonics that one wants, (ii) image the HHG and quantum trajectories in the *real*-time–frequency domain, and (iii) determine the carrier-envelope phase of the driving laser pulse.

DOI: 10.1103/PhysRevA.77.013405 PACS number(s): 32.80.Rm, 42.65.Re, 42.65.Ky

Measuring and controlling ultrafast processes is one of the exciting goals of scientists, e.g., femtochemistry has led to significant scientific advances [1]. In the past decade, there has been a great passion to extend to the attosecond domain. This is sprung by the finding of high-order harmonic generation (HHG), which has led to coherent soft x-ray sources and attosecond pulses [2,3]. It enables one to trace and control the electronic processes in atoms and molecules, leading to the beginning of attosecond physics. High-order harmonic spectrograms have been used to image the molecular orbitals with tomographic metrology [4], and attosecond pulses have also been used to observe the atomic inner-shell processes [5] and electron tunneling in atoms [6].

HHG is well understood in terms of the three-step model [7]. In detail, the electron is first ionized when atoms (or molecules) suffer the peak of the laser field (t_i marked in Fig. 1), then is accelerated in the laser field. Finally, the electron is driven back when the laser field reverses its direction, recombines with the parent ion at the zero transition of the laser field (t_r marked in Fig. 1) and then releases its energy by emitting coherent high-order harmonics. This process occurs periodically every half cycle, in which the electron takes two dominant classical trajectories (so-called short and long trajectories) of much different return times. The three-step model has been embodied in a quantum theory within the strong-field approximation (SFA) [8]. Employing the saddle point method, an intuitive understanding of the classical trajectory is demonstrated by the quantum trajectories. Salières *et al.* also interpreted this process with the Feynman path-integral approach [9], putting the three-step model to a more substantial basis. However, clear demonstration of the quantum trajectories is still an intractable issue in experiments. Can we image the trajectories in *real time*, and how?

In this work, we present a method to reconstruct the real-time–frequency image of HHG, connecting the theoretical quantum trajectories to the real spectrograms. Figure 1 shows the sketch of our scheme. To make the discussion concrete, we take helium as the target gas, and choose a Ti:sapphire laser pulse with a wavelength of 800 nm and an intensity of 3×10^{14} W/cm^2. It is much lower than the saturation intensity of helium, thus few helium is ionized ($\simeq$0.2%) in the near infrared (NIR) laser field alone. According to the three-step model, ionization is the starter of HHG. We therefore mix a trigger pulse to initiate the ionization and so the HHG. Due to the high photon energy and ultrashort duration, attosecond UV pulses are a robust tool to achieve this objective, which has been demonstrated in the quantum path control [10]. It should be emphasized that the electron motion should not be significantly affected by the UV pulse, otherwise the electron trajectory will be distorted. Hence we choose a weak UV pulse with a photon energy (9 eV, i.e., 135 nm for the central wavelength) much lower than the ionization threshold of helium (24.6 eV). Such a UV pulse will induce a transition to real or virtual excited state, facilitating optical-field ionization [11] and triggering the HHG, but make a negligible influence on the electron motion. After the ionization, the electron is accelerated in the laser field, and the kinetic energy is $[\int_{t_i}^{t_r}E(t)dt]^2/2$ where $E(t)$ is the electric field. Thus the laser field maps the electron motion in the energy domain, which will be inherited by the high-order harmonic spectrograms. Due to the short duration of the UV pulse, the ionization time is confined in an attosecond interval. Thus like an attosecond temporal filter (ATF), the UV pulse can select the high-order harmonics starting in an attosecond interval. By scanning the UV pulse, we can reconstruct the "snapshot" of HHG in the real-time–

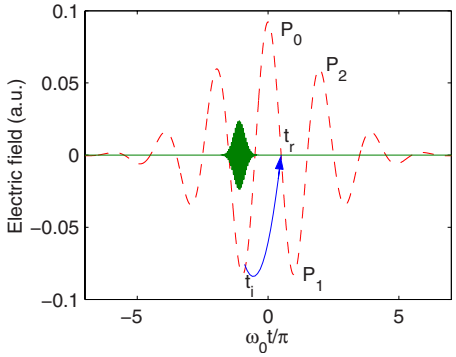

FIG. 1. (Color online) Schematic illustration of the high-order harmonic generation in the synthesized field of a NIR driving laser pulse and a UV attosecond pulse.

*Corresponding author. lupeixiang@mail.hust.edu.cn

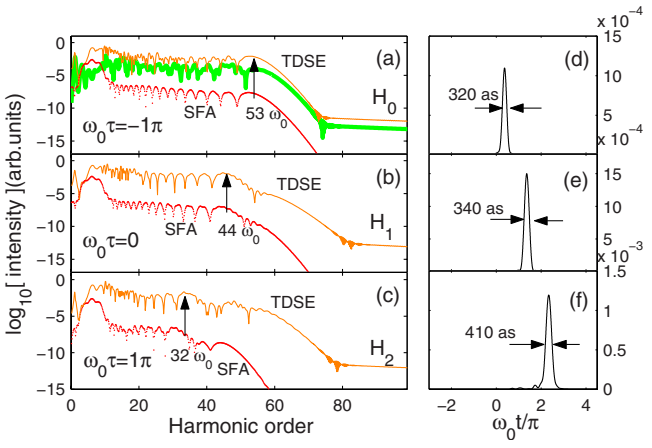

FIG. 2. (Color online) High-order harmonic spectra generated at the delays of (a) $\omega_0\tau=-\pi$, (b) 0, and (c) π. (d)–(f) show the attosecond pulses generated by filtering the cutoff high-order harmonics $50-60\omega_0$, $40-50\omega_0$, $30-40\omega_0$ shown in (a)–(c), respectively. The high-order harmonic spectrum in the driving NIR field alone is also shown in (a) (the bold green line). The intensity of the NIR laser pulse is 3×10^{14} W/cm^2, pulse duration is 5 fs, and the carrier-envelope phase is 0. For the UV pulse, the intensity is 2×10^{13} W/cm^2, the pulse duration is 1 fs.

frequency domain, which corresponds to the electron trajectories in the time-energy domain.

For the simulation, we solve the one dimensional time-dependent Schrödinger equation (TDSE) within the one-active-electron approximation. The electric field of the driving laser pulse is $E(t)=E_0f(t)\cos(\omega_0t+\phi_0)$ [in atomic units (a.u.)], where E_0 is the laser amplitude, $f(t)$ is the laser envelope, ω_0 is the frequency, and ϕ_0 is the carrier-envelope phase. A Gaussian envelope is adopted and the pulse duration of the laser pulse is 5-fs full width at half maximum. For the UV pulse, $E_{UV}(t)=E_{UV0}f(t-\tau)\cos[\omega_{UV}(t-\tau)]$ where τ is the delay between the NIR and UV pulses. The intensity of the UV pulse is 2×10^{13} W/cm^2 and the pulse duration is 1 fs. The time-dependent dipole acceleration can be calculated with the Ehrenfest theorem, and then the harmonic spectrum is calculated by Fourier transforming the dipole acceleration [12]. The thin line in Fig. 2(a) shows the harmonic spectrum recorded by ATF at $\omega_0\tau=-\pi$, and the bold line shows the HHG in the NIR laser pulse alone. One can see that the harmonic yield in the NIR pulse alone is one order of magnitude lower than that in the combination field. As the above discussion, the ionization probability is very low in NIR laser pulse alone, and the harmonic yield is low. While in the combined field, the ionization is triggered and enhanced nearly one order of magnitude by the UV pulse, and so the high-order harmonics are enhanced also. As shown by the thin line in Fig. 2(a), the harmonic spectrum shows a smooth plateau and then a cutoff at about $53\omega_0$. By synthesizing the cutoff high-order harmonics, an isolated attosecond pulse is generated at $\omega_0t=0.4\pi$ [Fig. 2(d)]. To reveal the electron trajectory associated with this high-order harmonic spectrum, we first analyze this process with the classical model. As in the above discussion, the electron is ionized in a short interval (several hundred attoseconds) near the peak of $\omega_0t_i=-\pi$, then is accelerated in the following half cycle. The maximum kinetic energy $[\int_{t_i}^{t_r}E(t)dt]^2/2 \simeq 3.2(E_{p0}/2\omega_0)^2$, where E_{p0} is the laser amplitude of peak P_0, is reached when $\omega_0t_i=-0.91\pi$. Finally, the electron recombines with the parent ion near the zero transition of the laser field (0.4π) by releasing its energy to high-order harmonics with the maximum energy of $I_p+3.2(E_{p0}/2\omega_0)^2 =2.98$ a.u.$\simeq53\omega_0$. All these properties agree well with the high-order harmonics (denoted as H_0) shown in Fig. 2(a), indicating that high-order harmonics H_0 are originated from the quantum trajectories in the half cycle P_0. By adjusting the delay, we can select the high-order harmonics associated with the electron trajectories in each half cycle, see Figs. 2(b) and 2(c) for the half cycle of P_1 and P_2, respectively. In other words, we can change the high-order harmonics by adjusting the UV pulse, indicating turnable high-order harmonic and attosecond pulse sources.

By scanning the UV pulse, we obtain the snapshot of HHG, which is shown in Fig. 3(a). One can clearly distinguish the high-order harmonics generated in each half cycle (H_0,$H_{\pm1}$). Interestingly, the cutoff energy of H_{-1} ($47\omega_0$) is higher than that of H_1 ($44\omega_0$), which is counterintuitive, since the laser amplitudes of P_{-1} and P_1 are equal. This is due to the nonadiabatic effect in the few-cycle regime. In detail, the NIR laser pulse increases rapidly in the ascend part, then the high-order harmonics are blueshifted [13]. On the contrary, high-order harmonics are redshifted in the descend part of the laser pulse. Shin *et al.* [13] only observed the HHG in the ascend laser pulse and Haworth *et al.* [14] did not clearly distinguish the high-order harmonics H_{-1} and H_1 yet, whereas ATF clearly records the HHG in each half cycle, which is the first time to the best of our knowledge, and so the nonadiabatic effects are explicitly demonstrated. In addition, as shown in Fig. 3(a), each half cycle harmonic shows a clear interference pattern. To understand this effect, we perform a simulation with the SFA model [8,15]. The dipole is given by

$$D(t)=\sum_{t_i}\frac{1}{\sqrt{i}}a_i(t_i)a_p(t_i,t_r)a_r(t_r) \quad (1)$$

which reflects the individual process participating in HHG, i.e., the electron is first set free at t_i with an ionization probability a_i, then propagates in the laser field accounted for by a_p, and finally recombines with the parent ion with a probability of a_r. In our scheme, the UV pulse promotes the ionization, the ionization probability is in proportion to $I_{UV}(t-\tau)$ [11], and then we assume that the ionization time is confined in an interval of the UV pulse duration. Note that this linear proportion of the ionization probability actually depends on the UV photon energy [11]. Our calculation shows that the ionization probability is linearly proportional to the UV pulse intensity near $\omega_{UV}=90$ nm (photon energy is about 13 eV) for our parameters, similarly to Ref. [11]. Apart from this wavelength, the linear proportion is slightly deviated, which, however, does not significantly influence our results. Also, we assume the UV pulse makes negligible influences on the electron motion and recombination probability; the other two terms are still kept as in Refs. [8,15]. The

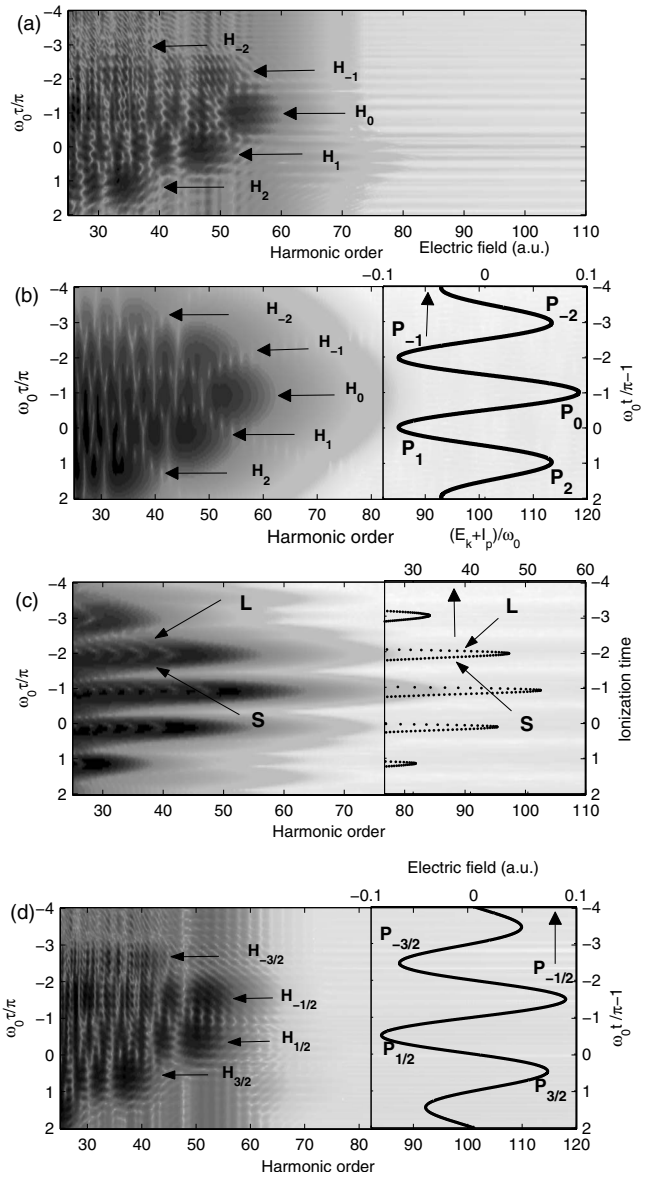

FIG. 3. High-order harmonic spectrogram as a function of the delay between the UV and the NIR laser pulse calculated with the (a) TDSE and (b) SFA model. The right plot in (b) shows the electric field of the NIR laser pulse. Note that the laser field is shifted by a phase of π for clearly connecting each peak to the harmonic spectra. (c) Same as (b), but with a UV pulse of 100 as. The right plot in (c) shows the dependence of the ionization time and kinetic energy E_k associated with different trajectories from the classical rescattering model. (d) Same as (a), but with a NIR pulse of $\phi_0 = 0.5\pi$. See Fig. S3 of EPAPS document No. E-PLRAAN-77–057801 for the color version.

high-order harmonic spectrum is calculated with the Fourier transform of the dipole,

$$H(\omega,\tau) = \mathcal{F}\left[\sum \frac{1}{\sqrt{i}} a_i(t-\tau)a_p a_r\right]. \tag{2}$$

In the calculation, only the quantum trajectories with travel times shorter than one optical cycle are considered; the other trajectories with longer travel times make a negligible contribution [9] (these trajectories only affect the lower order high-order harmonics and are suppressed in the few-cycle laser pulse). The high-order harmonic spectrum at $\omega_0\tau=-\pi$ is shown in Fig. 2(a) (dotted line), which agrees qualitatively with the result from TDSE. The travel time is confined in one optical cycle; we can clearly see that the harmonics H_0 are associated to the quantum trajectories in the half cycle of P_0, and H_1, H_2 correspond to those of P_1, P_2, respectively. The snapshot of HHG obtained with the SFA model is shown in Fig. 3(b). One can also see the interference pattern. According to the SFA model, there are two dominant quantum trajectories in each half cycle. The phases accumulated by the electron in different trajectories are different. The interference of these two trajectories gives rise to an evident modulation of the harmonic spectrum as shown in Figs. 3(a) and 3(b). This is analogous to Young's two-slit experiment. Our test simulation shows that by removing one trajectory, the interference pattern is really eliminated. In contrast to Fig. 3(b), the harmonic spectra show a slight oscillation in Fig. 3(a), which should be due to that the electron motion, ionization, and recombination probabilities are slightly influenced when scanning the UV pulse. This influence is neglected in the SFA calculation and oscillations are not present in Fig. 3(b).

Gabor transform (windowed Fourier transform) is an efficient numerical way to obtain the time-frequency image of HHG. It is defined as $H(\omega,\tau)=\mathcal{F}[D(t)W(t-\tau)]$. In the driving laser pulse alone, the time-frequency image is

$$H(\omega,\tau) = \mathcal{F}\left[\sum \frac{1}{\sqrt{i}} a_i a_p a_r W(t-\tau)\right]. \tag{3}$$

In this equation, a temporal window $W(t-\tau)$, which usually can be chosen as a Gaussian function, is applied to the dipole $D(t)$. After Fourier transform, the spectral property of the HHG in the temporal window can be obtained. From another point of view, we can equally say that a window function is applied to a_r, which confines the electron recombination time (i.e., the emission time of HHG) to a temporal window. By scanning the temporal window, the snapshot of the high-order harmonic generated in each temporal interval is obtained, reconstructing the time-frequency image of HHG. In our scheme of ATF, the UV pulse confines the ionization time in a short interval, acting as a temporal window to a_i. Similarly, by scanning the UV pulse, one can obtain the time-frequency image of HHG in the driving laser pulse. The only difference is that the UV pulse is applied to a_i, i.e., t in Eq. (2) is the ionization time, which is adjusted by scanning the delay of the UV pulse τ, and hence reconstructs the ionization time-frequency image of HHG. Whereas the window function in Gabor transform is applied to a_r, i.e., t in Eq. (3) is the recombination time [16], which is adjusted by changing the temporal window, and reconstructs the recombination time-frequency image. On the other hand, it is noteworthy to emphasize that Gabor transform is a numerical method, providing a *virtual* time-frequency image. On the contrary, the ATF records the HHG in the real-time–frequency domain. From this analogy, we can understand the above results more

conveniently. As shown in Fig. 2, one can select some specific high-order harmonics by adjusting the temporal window, i.e., UV pulse. And the duration of UV pulse is about 1 fs, the temporal resolution is ~ half cycle. Thus the high-order harmonics in each half cycle are clearly distinguished as shown in Fig. 3, from which we also observe the signature of the associated quantum trajectories, i.e., the interference pattern. In order to observe the subtle structure of quantum trajectories, we must improve the temporal resolution which can be achieved by reducing the UV pulse duration. If the ionization time is confined in 100 as, we can observe some fine structures in each half cycle high-order harmonics as shown in Fig. 3(c). For reference, we also show the dependence of the electron energy on the ionization time associated with each electron classical trajectory [right plot in Fig. 3(c)]. One can see that the subtle structures agree qualitatively with the classical model, indicating the short and long trajectories. Note that the electron trajectories can also be imaged from the recombination time of HHG by characterizing the attosecond emission [17], but the high-order harmonics generated in each half cycle were not distinguished in Ref. [17].

Figure 3(d) shows the snapshot of HHG in a laser pulse with the carrier-envelope phase of 0.5π. Compared to Fig. 3(a), one can clearly distinguish the high-order harmonics generated in each half cycle and the interference pattern. Also, it is shown that the harmonics $H_{\pm 1/2}$, $H_{\pm 3/2}$ are associated to the quantum trajectories in the optical cycles of $P_{\pm 1/2}$ and $P_{\pm 3/2}$, respectively. In addition, the high-order harmonics $H_{-1/2}$ are blueshifted, whereas $H_{1/2}$ is redshifted due to the nonadiabatic effect. All these properties agree well with the above discussions about Fig. 3(a). Thus our scheme of ATF is robust which works well at other carrier-envelope phases. We also investigate the influence of the fluctuation of the UV pulse. The results show that neither a variation of the intensity $(5\times 10^{12}-1\times 10^{14}\ \mathrm{W/cm^2})$ nor a variation of wavelength (80–150 nm) change the above results significantly.

In our scheme of ATF, the real-time–frequency image of HHG is constructed, which also contains the information of the driving laser pulse. Hence ATF also suggests a potential way to measure the carrier-envelope phase of the NIR laser pulse. As shown in Fig. 3(a), the time-frequency image shows the highest cutoff for high-order harmonics H_0 and another two shoulder harmonics $H_{\pm 1}$, which reflects the wave form of the cosine-shaped laser field. On the contrary, as shown in Fig. 3(d), the time-frequency image shows two highest-order harmonics $H_{\pm 1/2}$, which correspond to the sine-shaped laser pulse. From the half cycle harmonics, the carrier-envelope phase of the NIR pulse can be retrieved [14]. It is worth noting that the ATF can clearly distinguish the half cycle harmonics in a 10-fs laser pulse [16], suggesting a potential to extend the carrier-envelope phase measurement to the multicycle regime.

In summary, we present a different concept of ATF by mixing a weak UV pulse to a NIR laser pulse. It is shown that ATF constructs the real-time–frequency image of HHG, mapping the electron trajectories in the real-time–energy domain. With a 1-fs UV pulse, the high-order harmonics in each half cycle are clearly distinguished, from which we also observe the interference pattern of the associated quantum trajectories. By reducing the UV pulse duration, the temporal resolution can be improved, and the subtle structure of the quantum trajectory can be obtained with a temporal resolution of about 100 as. Note that our scheme seems feasible with the current instruments. Like Ref. [18], the 1-fs UV pulse can be produced using a few-cycle laser pulse, ensuring the observation of half cycle high-order harmonics. Further, the recent experiment has demonstrated the generation of a 130-as UV pulse using few-cycle laser pulses in combination with the polarization gating technique [19]. Also, it is shown that sub-100-as pulse can be produced with an ultrashort two-color field [20]. Such progresses facilitate the improvement of the temporal resolution and approach the observation of subtle structures of the quantum trajectories. In addition, ATF enables one to select the high-order harmonics in an attosecond interval. By adjusting the delay and UV pulse duration, one can select some specific high-order harmonics that one wants, indicating a tunable high-order harmonic and attosecond pulse sources. Moreover, ATF also suggests a potential way to measure the carrier-envelope phase of the multicycle laser pulse.

This work was supported by the National Natural Science Foundation of China under Grants No. 10574050, No. 10774054, No. 10734080, the "973" Foundation under Grant No. 2006CB806000, and the Specialized Research Fund for the Doctoral Program of Higher Education of China under Grant No. 20040487023.

[1] A. H. Zewail, J. Phys. Chem. A **104**, 5660 (2000).
[2] M. Hentschel *et al.*, Nature (London) **414**, 509 (2001).
[3] P. M. Paul *et al.*, Science **292**, 1689 (2001).
[4] J. Itatani *et al.*, Nature (London) **432**, 867 (2004).
[5] M. Drescher *et al.*, Nature (London) **419**, 803 (2002).
[6] M. Uiberacker *et al.*, Nature (London) **446**, 627 (2007).
[7] P. B. Corkum, Phys. Rev. Lett. **71**, 1994 (1993).
[8] M. Lewenstein, P. Balcou, M. Y. Ivanov, A. L'Huillier, and P. B. Corkum, Phys. Rev. A **49**, 2117 (1994).
[9] P. Salières *et al.*, Science **292**, 902 (2001).
[10] K. J. Schafer, M. B. Gaarde, A. Heinrich, J. Biegert, and U. Keller, Phys. Rev. Lett. **92**, 023003 (2004).
[11] K. Ishikawa, Phys. Rev. Lett. **91**, 043002 (2003).
[12] Pengfei Lan, Peixiang Lu, Wei Cao, Yuhua Li, and Xinlin Wang, Phys. Rev. A **76**, 021801(R) (2007).
[13] H. J. Shin, D. G. Lee, Y. H. Cha, K. H. Hong, and C. H. Nam, Phys. Rev. Lett. **83**, 2544 (1999).
[14] S. T. Cundiff, Nat. Phys. **3**, 16 (2007); C. A. Haworth, L. E. Chipperfield, J. S. Robinson, P. L. Knight, J. P. Marangos, and J. W. G. Tishch, *ibid.* **3**, 52 (2007).
[15] T. Brabec and F. Krausz, Rev. Mod. Phys. **72**, 545 (2000).
[16] See EPAPS Document No. E-PLRAAN-77-057801 for the

time-frequency image of HHG numerically obtained with Gabor transform (Fig. S1) and the snapshot of HHG in a 10–fs laser pulse (Fig. S2). For more information on EPAPS, see http://www.aip.org/pubservs/epaps.html.

[17] Y. Mairesse *et al.*, Science **302**, 1540 (2003).

[18] R. Kienberger *et al.*, Nature (London) **427**, 817 (2004).

[19] G. Sansone *et al.*, Science **314**, 443 (2006).

[20] Z. N. Zeng, Y. Cheng, X. Song, R. X. Li, and Z. Z. Xu, Phys. Rev. Lett. **98**, 203901 (2007); P. F. Lan, P. X. Lu, W. Cao, Y. H. Li, and X. L. Wang, Phys. Rev. A **76**, 011402(R) (2007).